IMREPET: Implicit Neural Representation for Unsupervised Dynamic PET Reconstruction

Kailong Fan[1], Yubo Ye[1], Huafeng Liu[1⋆], and Linwei Wang[2]

[1] State Key Laboratory of Extreme Photonics and Instrumentation, Department of Optical Engineering, Zhejiang University, Hangzhou 310027, China
liuhf@zju.edu.cn
[2] Rochester Institute of Technology, Rochester, NY 14623, USA
linwei.wang@rit.edu

Abstract. Deep image prior (DIP) has become an important approach to unsupervised reconstruction of Positron Emission Tomography (PET) images. In the setting of dynamic PET, however, its performance is limited by the frame-by-frame reconstruction, computational cost, and the fixed-size discrete representation of PET images. To address these challenges, we propose IMREPET, a novel dynamic PET reconstruction method based on implicit neural networks (INR). By incorporating temporal information directly into INR's parameterization of dynamic PET images, we overcome the limitation of frame-by-frame reconstructions without the need of complex algorithms or regularization. Results on simulated and real-data experiments showed that IMREPET enabled rapid, high-quality reconstruction with improved signal-to-noise ratio and enhanced image detail recovery, while drastically reducing computation time compared to DIP baselines. The resolution-agnostic nature of INR further allowed IMREPET to reconstruct PET images at any resolution. These results show the feasibility of IMREPET as a robust and efficient solution for dynamic PET imaging.

Keywords: implicit neural representation · dynamic PET reconstruction

1 Introduction

Dynamic PET images provide detailed insights into the spatial and temporal distribution of radiotracers within the human body, facilitating quantitative analyses such as physiological parameter estimation [7, 2]. However, due to the ill-conditioned problem and low counting statistics, dynamic PET reconstruction remains challenging [27, 18]. Traditional methods generally employ frame-by-frame reconstructions which, such as the Maximum Likelihood Expectation Maximization (MLEM) [13], tend to overfit to noises in the data. Although improvements such as kernel methods [28] have been proposed to enhance reconstruction by incorporating prior knowledge, their reliance on the accuracy of prior knowledge limits their widespread applicability [19].

⋆ Corresponding author: liuhf@zju.edu.cn

In recent years, deep learning has been increasingly integrated into PET reconstruction. Most approaches, whether via end-to-end direct reconstruction [10, 29] or unrolled iterative optimizations [9, 16], require supervised training using high-quality datasets that are costly to obtain in PET imaging. For unsupervised PET reconstruction, deep image prior (DIP) [26] has been widely used to exploit the inherent prior of a CNN with PET reconstruction [6, 11]. While most of these methods focus on frame-by-frame reconstruction neglecting temporal information [14, 15], multiple DIP networks have been utilized with Non-negative Matrix Factorization (NMF) to separately reconstruct the spatial and temporal distributions of PET concentration [32]. This approach however introduces additional regularization terms and iterative steps, making model optimization more challenging. Additionally, due to the discrete spatial representation of PET images with CNNs, it generally requires the cropping of input images [6, 10]. Furthermore, as the depth and number of CNNs in the DIP model increase, the computational cost also becomes prohibitively high.

Implicit Neural Representation (INR) is a image representation method that has gained significant recent attention. INR uses implicit continuous functions to represent objects, with the continuous function being parameterized by a multilayer perceptron (MLP) [25, 24, 20]. This continuous function representation has shown a strong capability in capturing image priors [23], as well as remarkable results in CT [30, 25] and MRI [4, 31] imaging. The use of INR in PET reconstruction, however, has not been attempted.

In this paper, we propose the first framework of IMplicit neural REpresentation for dynamic PET reconstruction (IMREPET). By replacing the DIP and other image priors with an INR prior to represent PET activity images, we improve the generalizability and reduce the complexity for unsupervised PET image reconstruction. Moreover, by incorporating temporal information directly into INR's parameterization of dynamic PET images, we overcome the limitation of frame-by-frame reconstructions without introducing complex algorithms or regularization. Our main contribution includes 1) exploring the first application of INR to improve the reconstruction of dynamic PET image, 2) presenting an unsupervised and learning-free approach that does not require any prior images and can be applied to different organs, 3) significantly reducing computation time compared to DIP-based methods, and 4) being able to handle image reconstruction at any resolution, including achieving super-resolution during reconstructions. We demonstrated the above benefits of IMREPET in a comprehensive set of synthetic and real data experiments, in comparison to existing unsupervised approaches to dynamic PET recontruction.

2 Methods

Problem Formulation: In dynamic PET image reconstruction, the measured sinogram $\boldsymbol{y}_t \in \mathbb{R}^M$ at time frame t can be regarded as a set of independent random variables that follows Poisson distribution, with its mean value as:

$$\bar{\boldsymbol{y}}_t = \boldsymbol{P}\boldsymbol{x}_t + \boldsymbol{r}_t, \quad t = 1, \cdots, T \tag{1}$$

where $\boldsymbol{P} \in \mathbb{R}^{M \times N}$ is the transformation matrix of PET system, $\boldsymbol{x}_t \in \mathbb{R}^N$ is the activity image that represents the spatial distribution of tracer radioactivity at t, and $\boldsymbol{r}_t \in \mathbb{R}^M$ is a noise term that denotes random and scattered events. M and N are the total number of pixels of sinogram and PET image respectively, and T is the number of time frames. When $\boldsymbol{y}_t$ follows Poisson distribution $p\left(\boldsymbol{y}_t|\boldsymbol{x}_t\right)$, the log likelihood function for the measured data $\boldsymbol{y}_{1:T}$ can be represented as:

$$\mathcal{L}\left(\boldsymbol{y}_{1:T}|\boldsymbol{x}_{1:T}\right) = \sum_{t=1}^{T}\sum_{i=1}^{M} logp\left(y_{i,t}|\boldsymbol{x}_t\right) = \sum_{t=1}^{T}\sum_{i=1}^{M} y_{i,t} log\bar{y}_{i,t} - \bar{y}_{i,t} - logy_{i,t}! \quad (2)$$

INR of Dynamic PET images: We use INR to model a PET image as a continuous function of the spatial coordinates c. We use the multi-channel outputs of INR to represent time information of dynamic PET images as $\boldsymbol{x}_{1:T} = f_\theta\left(c\right)$, where the INR network f_θ is modled as a multi-layer perceptron (MLP) with ReLU activations followed by a sigmoid activation, parameterized by θ. In Section 3.3, we ablate this design choice *vs.* incorporating time t as an additional input to INR. Due to the MLP's tendency to favor low-frequency information of images, we use Fourier feature mapping to let the network learn high-frequency information. The process of Fourier feature encoding can be described as: $\gamma(c) = \left[\cos(2\pi c\boldsymbol{B}), \sin(2\pi c\boldsymbol{B})\right]^\top$, where $\boldsymbol{B} \in \mathbb{R}^{2\times G}$ is a random Gaussian matrix following a normal distribution $\mathcal{N}(0,1)$, and G is the number of Fourier feature dimensions. In IMREPET, we set $G = 256$ for all experiments based on ablation shown in Section 3.3. Dynamic PET images can now be represented as:

$$\boldsymbol{x}_{1:T} = f_\theta\left(\gamma(c)\right) = f_\theta\left(\left[\cos(2\pi c\boldsymbol{B}), \sin(2\pi c\boldsymbol{B})\right]^\top\right) \quad (3)$$

Optimization: When substituting Equation (3) in Equation (1), the log likelihood function can be expressed using f_θ as:

$$\mathcal{L}(\boldsymbol{y}_{1:T}|\boldsymbol{x}_{1:T};\theta) = \sum_{i=1}^{M} logp\left(y_{i,1:T}|f_\theta\left(\left[\cos(2\pi c\boldsymbol{B}), \sin(2\pi c\boldsymbol{B})\right]^\top\right)\right) \quad (4)$$

Given observed sinograms, we reconstruct $\boldsymbol{x}_{1:T}$ by minimizing Equation (4) as:

$$\hat{\theta} = \arg\min_\theta\{-\mathcal{L}(\boldsymbol{y}_{1:T}|\boldsymbol{x}_{1:T};\theta)\}, \quad \hat{\boldsymbol{x}}_{1:T} = f_{\hat{\theta}}\left(\left[\cos(2\pi c\boldsymbol{B}), \sin(2\pi c\boldsymbol{B})\right]^\top\right) \quad (5)$$

Fig. 1 summarizes the proposed framework.

3 Experiments and Results

3.1 Data

Brain Data Simulation. A brain phantom from BrainWeb [1] was used to generate simulation dynamic PET data. The pixel size was 2×2 mm^2 and

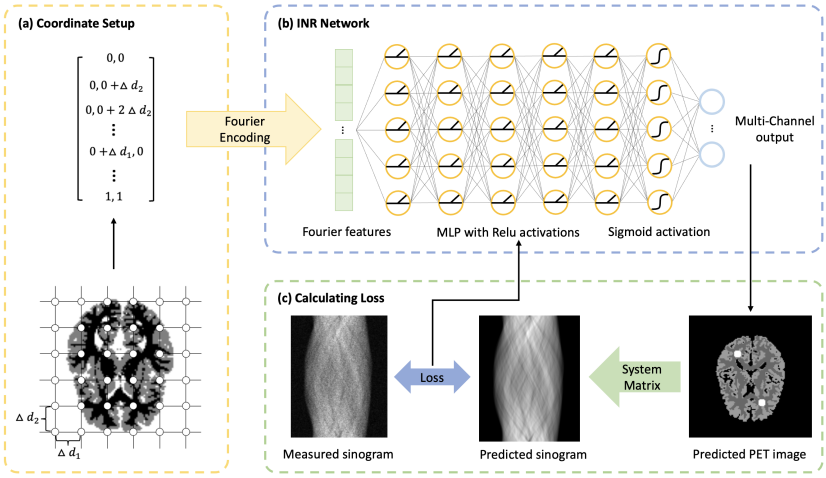

Fig. 1. Overview of IMREPET. (a) Construct Fourier feature map of coordinates. (b) The INR network. (c) The forward process from PET images to measured sinograms.

the phantom size was 128×128. Two 16 mm hot spheres were inserted into the PET image as tumor ROIs. Two-compartmental model with Feng's input function was adopted to simulate dynamic ^{18}F-FDG scans [3]. The ground truth of time activity curves of blood, gray matter, white matter, and tumor were simulated using kinetic parameters from [7]. The scanning schedule consisted of 18 time frames over 60 min: 3×60 s, 9×180 s, 6×300 s. The system matrix was computed by using Michigan Image Reconstruction Toolbox (IRT) with a simple strip-integral model [5]. The number of detector bins and projection angles were 128 and 160. Poisson noise was added to the simulated sinograms with the total count number at $\sim 1.8\times 10^7$. Uniform random events were simulated to account for 20% of the noise-free data. Scattered events were not included.

Thorax Data Simulation. We used human XCAT digital phantom to generate thorax data [22]. The pixel size was 3×3 mm^2 and the phantom size was 128×128. Similarly, we used two-compartmental model with Feng's input function to generate the ground truth of dynamic PET image. The kinetics parameters were adopted from [8]. We simulated ROIs including myocardium, liver, lung, pancreas, marrow, muscle, bone, and soft tissue. The sinograms were generated as described above and the total count number was set at approximately 1.2×10^7.

Real Patient Data. A 65-minutes scan with a scan length of 106 cm of a patient obtained from Biograph Vision Quadra was used [17]. The dimension of the images was $440 \times 440 \times 645$ with $1.65 \times 1.65 \times 1.65$ mm^3. The data were divided into 62 time frames with the schedule 2×10 s, 30×2 s, 4×10 s, 8×30 s, 4×60 s, 5×120 s, 9×300 s. The images were reconstructed using the manufacturer's standard reconstruction technique involving point spread function

Table 1. Metrics of reconstructed PET images on simulated brain and thorax data

Dataset	Methods	MSE (%) ↓	PSNR (dB) ↑	SSIM ↑
Brain	MLEM	0.51 ± 0.02	22.97 ± 0.18	0.81 ± 0.01
	KEM	0.30 ± 0.02	25.18 ± 0.28	0.88 ± 0.00
	DIPNMF	0.20 ± 0.03	26.96 ± 0.64	0.93 ± 0.01
	IMREPET(Proposed)	$\mathbf{0.11 \pm 0.01}$	$\mathbf{29.46 \pm 0.30}$	$\mathbf{0.95 \pm 0.00}$
Thorax	MLEM	0.10 ± 0.01	30.10 ± 0.43	0.85 ± 0.03
	KEM	0.07 ± 0.01	31.73 ± 0.84	0.92 ± 0.01
	DIPNMF	0.09 ± 0.01	30.60 ± 0.68	0.93 ± 0.01
	IMREPET(Proposed)	$\mathbf{0.02 \pm 0.01}$	$\mathbf{36.97 \pm 1.96}$	$\mathbf{0.97 \pm 0.01}$

modeling combined with time-of-flight (PSF+TOF OSEM, 4 iterations × 5 subsets), followed by Gaussian post-filtering (2 mm FWHM) [12, 21], which were regarded as the ground truth. To reduce GPU memory, we resized the images to $128 \times 128 \times 300$. Since we did not obtain the system matrix of the instrument, we used IRT to generate sinograms following the same process as described above.

3.2 Models and Metrics

Implementation Details. For all PET reconstruction results presented in this paper, we used Adam optimizer with a learning rate of 10^{-3} and a decay ratio of 0.98 every 30 iterations. We used gradient clipping with a norm value of 1.0. Based on empirical results, we set the number of training iterations to 3000, to balance the utilization of the INR's inherent priors and avoiding fitting the noise. The optimization was performed on an NVIDIA Quadro RTX 8000 GPU.

Baselines. We consider three different reconstruction baselines: standard ML-EM, Kernel methods (KEM) [28], and NMF incorporated with DIP (DIPNMF) [32]. KEM integrates kernel matrix derived from prior knowledge into the EM process, where we generate the kernel matrix as in [28]. DIPNMF employs multiple CNNs to model the spatial distribution of PET data and an EM-based multiplicative update rule for temporal refinement. We adopt its publicly-released implementation with the same parameter settings as in the published paper. The number of iterations were empirically tuned for each baseline for best results.

Evaluation Metrics. We adopted mean squared error (MSE), peak signal-to-noise ratio (PSNR) and the structural similarity index measure (SSIM) to evaluate the reconstructed images. For ROI quantification and bias variance analysis, we adopt the bias and standard deviation (SD) in ROIs as:

$$\text{Bias} = \frac{1}{v_{\text{true}}}|\bar{v} - v_{\text{true}}|, \quad \text{SD} = \frac{1}{v_{\text{true}}}\sqrt{\frac{1}{D-1}\sum_{i=1}^{D}|v_i - \bar{v}|}, \bar{v} = \frac{1}{D}\sum_{i=1}^{D} v_i \tag{6}$$

where v_{true} is the ground truth of ROI uptake, D is the number of test samples set to 20, v_i is the mean ROI uptake in the ith test sample.

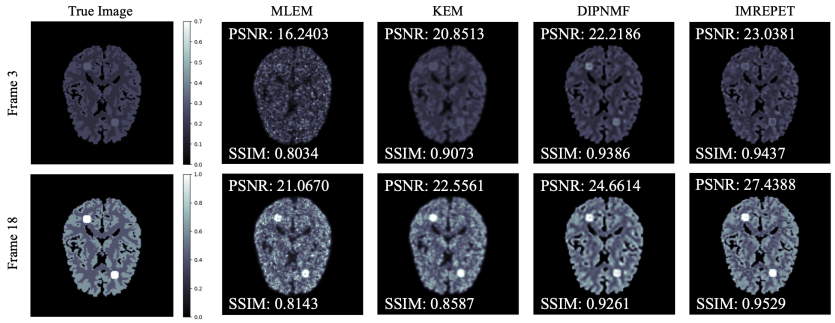

Fig. 2. Ground-truth and reconstructed PET images on simulated brain data, at frame 3 (low count) and 18 (relatively high count).

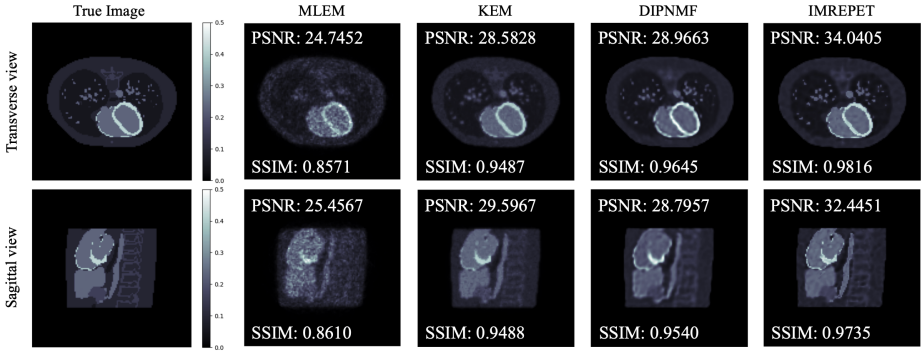

Fig. 3. Ground-truth and reconstructed PET images on simulated thorax data.

3.3 Results

Results on Simulation Data. The quantitative metrics on both the brain and thorax data are summarized in Table 1 with their respective visual examples provided in Fig. 2 and Fig. 3. The PSNR and SSIM values annotated in the figure are calculated for a single frame. In all results, as expected, KEM improved MLEM yet still suffered from noises. DIPNMF further reduced noised, but led to over-smoothness. In comparison, IMREPET achieved both reduced noises due to the continuous INR representation, as well as improved details owing to the ability of Fourier feature encoding to capture high-frequency information.

In terms of computation cost, without using neural networks as priors, ML-EM and KEM required the least time (less than 10 seconds). DIPNMF, built on the U-Net architecture, consumed approximately 1.7 hours to produce satisfactory results. In contrast, IMREPET required less than 100 seconds to achieve higher-quality results, highlighting its computational efficiency.

Fig. 4 presents the trade-off curves between the bias and SD on the tumor ROI region. The curves were calculated by varying the iteration number from 40 to 100 with an interval of 10 for ML-EM and KEM, 8000 to 20000 with an interval of 2000 for DIPNMF, 1200 to 3000 with an interval of 300 for IMREPET. As

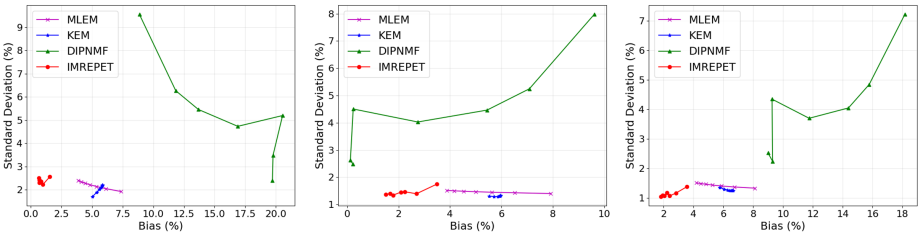

Fig. 4. Bias-SD trade-off for tumor ROI. Left to right: frame 3, 10, and 18.

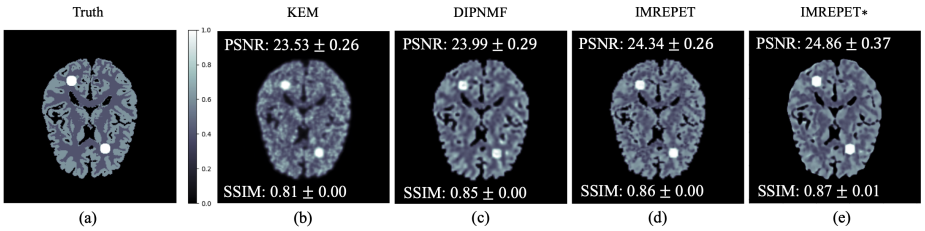

Fig. 5. Results of super-resolution. (a): True activity image with size of 256×256. (b)-(d): 256×256 images obtained by interpolating the reconstructed 128×128 images. (e) 256×256 images directly obtained from the INR in IMREPET.

shown, the bias decreased as the iteration number increased (*i.e.*, from rightmost to leftmost on each curve) for all methods. DIPNMF exhibited the largest bias in frames 3 and 18. Although it achieved the smallest bias in frame 10, its SD was the largest across all frames, demonstrating poor bias-SD balance. In comparison, IMREPER achieved the lowest bias and SD in frame 18, the lowest SD with relatively low bias in frame 10, and the lowest bias with relatively low SD in frame 3, demonstrating improved bias-SD trade-off in the tumor ROI.

Super-Resolution Experiments. A well-known characteristic of INR is its ability to achieve infinite resolution. To validate this feature, we generated simulated activity images with a resolution of 256×256. We subsequently downsampled them to 128×128 and derived sinograms from these low-resolution activity images for reconstruction. Fig. 5(b)-(d) illustrate 256×256 images obtained from 128×128 reconstructions from all methods using bilinear interpolation. Fig. 5(e) shows the 256×256 image directly generated from the optimized INR. The quantitative values calculated from 20 test samples demonstrated the improved super-resolution ability of IMREPET.

Result of Real Patient Data: Fig. 6 shows the reconstructed images on the real patient data. As expected, reconstruction results from ML-EM contained a significant amount of noises. KEM reduced the noise considerably in the thorax reconstruction, but not effective in the brain reconstruction. DIPNMF produced much smoother images, but the brain reconstruction exhibited artifacts while

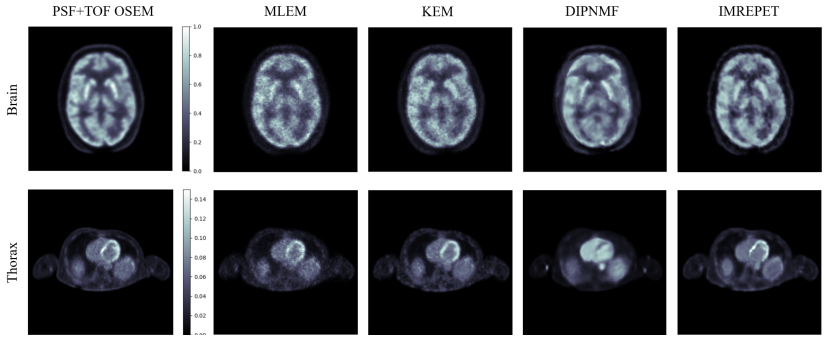

Fig. 6. Reconstruction results of real patient data.

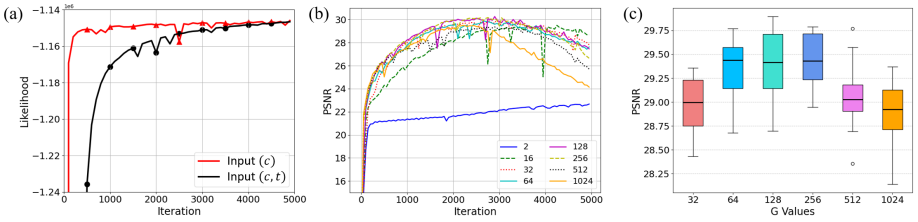

Fig. 7. (a) Convergence of IMREPET with and without t as input to INR. (b) Changes of PSNR with the number of iterations and (c) PSNR box-plots, with different G values.

the heart region in the thorax reconstruction was inaccurate. This may be due to the model's complexity and limited generalizability. DIPNMF involves multiple U-Nets and many hyperparameters that require manual tuning. For fair comparison, we used the same parameters across all subjects, which may have led to suboptimal trade-offs. This also helps explain DIPNMF's subpar performance in the bias–SD trade-off evaluation on the simulated brain dataset. In contrast, IMREPET effectively reduced noise while maintaining excellent detail preservation.

Ablation studies: Fig. 7(a) shows the log-likelihood curve of IMREPET with and without time t as an input to the INR on the simulated brain data, including only the portion when log-likelihood values $> -1.24 \times 10^6$. It can be observed that the log-likelihood converged faster when t was not modeled as an input to INR. Fig. 7(b) tracks PSNR values over iterations when using different G values in Fourier feature encoding on the simulated brain data, with $G = 2$ implying no Fourier feature encoding. It indicated that INR, similar to DIP, first learns the natural features of the image and then gradually fits the noises. We thus set the number of iterations to 3000 with a learning rate decay of 0.98 every 30 iterations, and tested the effects of different G values on 20 simulated brain data samples, as shown in the Fig. 7(c). Main results reported earlier used $G = 256$.

Discussion and Conclusion. We presented the first INR-based approach to dynamic PET reconstruction. Our results showed that IMREPT bridged the gap between traditional iterative methods (efficient but noise-prone) and recent DIP-based methods (over-smoothed and computationally expensive) to produce smooth reconstructions with enhanced detail preservation and efficient computation. Its resolution-agnostic nature further opens up opportunities for high-resolution imaging and super-resolution tasks. Future work will focus on extending IMREPET to handle real-world clinical datasets and exploring its integration into clinical workflows to enhance PET imaging and diagnostic capabilities.

Acknowledgments. This work is supported in part by the National Natural Science Foundation of China (No:62427807); NIH National Heart, Lung, and Blood Institute (NHLBI) grant R01HL145590.

Disclosure of Interests. The authors have no competing interests to declare that are relevant to the content of this article.

References

1. Aubert-Broche, B., Griffin, M., Pike, G.B., Evans, A.C., Collins, D.L.: Twenty new digital brain phantoms for creation of validation image data bases. IEEE transactions on medical imaging **25**(11), 1410–1416 (2006)
2. Dimitrakopoulou-Strauss, A., Pan, L., Sachpekidis, C.: Kinetic modeling and parametric imaging with dynamic pet for oncological applications: general considerations, current clinical applications, and future perspectives. European journal of nuclear medicine and molecular imaging **48**, 21–39 (2021)
3. Feng, D., Wong, K.P., Wu, C.M., Siu, W.C.: A technique for extracting physiological parameters and the required input function simultaneously from pet image measurements: Theory and simulation study. IEEE transactions on information technology in biomedicine **1**(4), 243–254 (1997)
4. Feng, R., Wu, Q., Feng, J., She, H., Liu, C., Zhang, Y., Wei, H.: Imjense: scan-specific implicit representation for joint coil sensitivity and image estimation in parallel mri. IEEE Transactions on Medical Imaging (2023)
5. Fessler, J.A.: Penalized weighted least-squares image reconstruction for positron emission tomography. IEEE transactions on medical imaging **13**(2), 290–300 (1994)
6. Gong, K., Catana, C., Qi, J., Li, Q.: Pet image reconstruction using deep image prior. IEEE transactions on medical imaging **38**(7), 1655–1665 (2018)
7. Gong, K., Cheng-Liao, J., Wang, G., Chen, K.T., Catana, C., Qi, J.: Direct patlak reconstruction from dynamic pet data using the kernel method with mri information based on structural similarity. IEEE transactions on medical imaging **37**(4), 955–965 (2017)
8. Gong, K., Guan, J., Kim, K., Zhang, X., Yang, J., Seo, Y., El Fakhri, G., Qi, J., Li, Q.: Iterative pet image reconstruction using convolutional neural network representation. IEEE transactions on medical imaging **38**(3), 675–685 (2018)
9. Gong, K., Wu, D., Kim, K., Yang, J., El Fakhri, G., Seo, Y., Li, Q.: Emnet: an unrolled deep neural network for pet image reconstruction. In: Medical imaging 2019: Physics of medical imaging. vol. 10948, pp. 1203–1208. SPIE (2019)

10. Häggström, I., Schmidtlein, C.R., Campanella, G., Fuchs, T.J.: Deeppet: A deep encoder–decoder network for directly solving the pet image reconstruction inverse problem. Medical image analysis **54**, 253–262 (2019)
11. Hashimoto, F., Ote, K., Onishi, Y.: Pet image reconstruction incorporating deep image prior and a forward projection model. IEEE Transactions on Radiation and Plasma Medical Sciences **6**(8), 841–846 (2022)
12. Hu, J., Panin, V., Smith, A.M., Spottiswoode, B., Shah, V., von Gall, C.C., Baker, M., Howe, W., Kehren, F., Casey, M., et al.: Design and implementation of automated clinical whole body parametric pet with continuous bed motion. IEEE Transactions on Radiation and Plasma Medical Sciences **4**(6), 696–707 (2020)
13. LA, S.: Maximum likelihood reconstruction for emission tomography. IEEE Trans Med Imaging **1**(2), 112–113 (1982)
14. Li, S., Gong, K., Badawi, R.D., Kim, E.J., Qi, J., Wang, G.: Neural kem: A kernel method with deep coefficient prior for pet image reconstruction. IEEE transactions on medical imaging **42**(3), 785–796 (2022)
15. Li, S., Wang, G.: Deep kernel representation for image reconstruction in pet. IEEE transactions on medical imaging **41**(11), 3029–3038 (2022)
16. Mehranian, A., Reader, A.J.: Model-based deep learning pet image reconstruction using forward–backward splitting expectation–maximization. IEEE transactions on radiation and plasma medical sciences **5**(1), 54–64 (2020)
17. Prenosil, G.A., Sari, H., Fürstner, M., Afshar-Oromieh, A., Shi, K., Rominger, A., Hentschel, M.: Performance characteristics of the biograph vision quadra pet/ct system with a long axial field of view using the nema nu 2-2018 standard. Journal of nuclear medicine **63**(3), 476–484 (2022)
18. Qi, J., Leahy, R.M.: Iterative reconstruction techniques in emission computed tomography. Physics in Medicine & Biology **51**(15), R541 (2006)
19. Reader, A.J., Pan, B.: Ai for pet image reconstruction. The British journal of radiology **96**(1150), 20230292 (2023)
20. Saragadam, V., LeJeune, D., Tan, J., Balakrishnan, G., Veeraraghavan, A., Baraniuk, R.G.: Wire: Wavelet implicit neural representations. In: Proceedings of the IEEE/CVF Conference on Computer Vision and Pattern Recognition. pp. 18507–18516 (2023)
21. Sari, H., Mingels, C., Alberts, I., Hu, J., Buesser, D., Shah, V., Schepers, R., Caluori, P., Panin, V., Conti, M., et al.: First results on kinetic modelling and parametric imaging of dynamic 18 f-fdg datasets from a long axial fov pet scanner in oncological patients. European journal of nuclear medicine and molecular imaging pp. 1–13 (2022)
22. Segars, W.P., Sturgeon, G., Mendonca, S., Grimes, J., Tsui, B.M.: 4d xcat phantom for multimodality imaging research. Medical physics **37**(9), 4902–4915 (2010)
23. Shen, L., Pauly, J., Xing, L.: Nerp: implicit neural representation learning with prior embedding for sparsely sampled image reconstruction. IEEE Transactions on Neural Networks and Learning Systems **35**(1), 770–782 (2022)
24. Sitzmann, V., Martel, J., Bergman, A., Lindell, D., Wetzstein, G.: Implicit neural representations with periodic activation functions. Advances in neural information processing systems **33**, 7462–7473 (2020)
25. Tancik, M., Srinivasan, P., Mildenhall, B., Fridovich-Keil, S., Raghavan, N., Singhal, U., Ramamoorthi, R., Barron, J., Ng, R.: Fourier features let networks learn high frequency functions in low dimensional domains. Advances in neural information processing systems **33**, 7537–7547 (2020)
26. Ulyanov, D., Vedaldi, A., Lempitsky, V.: Deep image prior. In: Proceedings of the IEEE conference on computer vision and pattern recognition. pp. 9446–9454 (2018)

27. Wang, B., Liu, H.: Fbp-net for direct reconstruction of dynamic pet images. Physics in Medicine & Biology **65**(23), 235008 (2020)
28. Wang, G., Qi, J.: Pet image reconstruction using kernel method. IEEE transactions on medical imaging **34**(1), 61–71 (2014)
29. Whiteley, W., Panin, V., Zhou, C., Cabello, J., Bharkhada, D., Gregor, J.: Fastpet: near real-time reconstruction of pet histo-image data using a neural network. IEEE Transactions on Radiation and Plasma Medical Sciences **5**(1), 65–77 (2020)
30. Wu, Q., Feng, R., Wei, H., Yu, J., Zhang, Y.: Self-supervised coordinate projection network for sparse-view computed tomography. IEEE Transactions on Computational Imaging **9**, 517–529 (2023)
31. Wu, Q., Li, Y., Xu, L., Feng, R., Wei, H., Yang, Q., Yu, B., Liu, X., Yu, J., Zhang, Y.: Irem: High-resolution magnetic resonance image reconstruction via implicit neural representation. In: Medical Image Computing and Computer Assisted Intervention–MICCAI 2021: 24th International Conference, Strasbourg, France, September 27–October 1, 2021, Proceedings, Part VI 24. pp. 65–74. Springer (2021)
32. Yokota, T., Kawai, K., Sakata, M., Kimura, Y., Hontani, H.: Dynamic pet image reconstruction using nonnegative matrix factorization incorporated with deep image prior. In: Proceedings of the IEEE/CVF international conference on computer vision. pp. 3126–3135 (2019)